Progress in Physics of Applied Materials 6 (2026), Serial Number 12, 229-238

Semnan University

Progress in Physics of Applied Materials

journal homepage: https://ppam.semnan.ac.ir/

Structural and Magnetic Properties of Pb-substituted $CuFe_2O_4$ Nanoparticles

Sanaz Rezaei [a], Ahmad Gholizadeh [a,*], Muhammad Atif [b]

[a] *School of Physics, Damghan University, Damghan, Iran*
[b] *Functional Materials Lab, Department of Physics, Air University, PAF Complex E-9, Islamabad, Pakistan*

ARTICLE INFO

Article history:
Received: 21 October 2025
Revised: 8 January 2026
Accepted: 21 January 2026
Published online: 18 February 2026

Keywords:
Spinel Ferrite;
$CuFe_2O_4$;
Sol–gel auto-combustion route;
FTIR;
Magnetic behavior.

ABSTRACT

Lead-substituted copper ferrites ($Cu_{1-x}Pb_xFe_2O_4$, x = 0.0–0.30) were synthesized via a sol–gel auto-combustion route to explore the structural and magnetic effects of Pb^{2+} incorporation. X-ray diffraction confirmed a tetragonal spinel phase ($I4_1/amd$) for low Pb content, which gradually evolved into a pseudo-cubic structure at higher substitution levels. The lattice parameters increased systematically with Pb doping, indicating lattice expansion and suppression of Jahn–Teller distortion. FTIR spectra revealed a red shift of both tetrahedral and octahedral metal–oxygen stretching modes, consistent with elongation of M–O bonds and partial Pb^{2+} occupancy of both sites. Magnetic measurements showed soft-ferromagnetic behavior with a notable increase in saturation magnetization (M_s) up to x = 0.25, followed by a decrease at higher Pb levels due to secondary phase formation and lattice strain. The reduction in coercivity (H_c) with Pb content reflects a weakening of magnetocrystalline anisotropy and lattice relaxation. These results highlight the structural flexibility and magnetic tunability of Pb-substituted $CuFe_2O_4$, emphasizing the role of large, nonmagnetic cations in controlling spinel ferrite functionality.

1. Introduction

Spinel ferrites, with the general formula MFe_2O_4 (where M = Cu, Co, Ni, Zn, etc.), constitute a highly versatile class of materials exhibiting diverse magnetic, electrical, and catalytic properties [1-4]. Their fundamental structure comprises two interpenetrating sublattices: tetrahedral (A) and octahedral (B) sites occupied by cations, with oxygen forming a close-packed cubic array. The interplay between these sites through superexchange interactions (A–O–B and B–O–B) governs the net magnetic and structural behavior of the spinel lattice [5–9]. Copper ferrite ($CuFe_2O_4$) is particularly notable for its Jahn–Teller distortion, arising from the degenerate eg orbitals of Cu^{2+} ($3d^9$). This distortion stabilizes a tetragonal spinel structure below 600 °C, which transforms into a cubic structure at elevated temperatures [10-13]. The tetragonal distortion affects both cation distribution and magnetic anisotropy. In the normal spinel configuration, Cu^{2+} predominantly occupies octahedral (B) sites, while Fe^{3+} ions are distributed across both A and B sites in varying ratios depending on the synthesis route and annealing conditions. Cation substitution at the M^{2+} site is a powerful strategy to tune ferrite properties. Incorporation of ions with different valence states and ionic radii alters lattice symmetry, exchange interactions, and electrical transport [14–17]. For instance, Co^{2+} substitution in $CuFe_2O_4$ enhances coercivity due to stronger spin–orbit coupling, while Gd^{3+} incorporation increases magnetocrystalline anisotropy and lattice strain [18-19]. Zn^{2+} and Ni^{2+} substitutions have been shown to modify conductivity and saturation magnetization [20–21]. However, Pb^{2+} substitution has been

* Corresponding author.
E-mail address: gholizadeh@du.ac.ir.

Cite this article as:
Rezaei, S., Gholizadeh, A. and Atif, M., 2026. Structural and Magnetic Properties of Pb-substituted $CuFe_2O_4$ Nanoparticles, *6*(3), pp.229-238. DOI: 10.22075/ppam.2026.39461.1178

comparatively less explored, despite its large ionic radius (1.29 Å) and nonmagnetic ($6s^2$) configuration, which can induce significant lattice distortions and modify the magnetostructural balance. The present study investigates $Cu_{1-x}Pb_xFe_2O_4$ nanoparticles synthesized via a sol–gel auto-combustion route, a method known for producing homogeneous and fine-grained powders. By focusing exclusively on Pb^{2+} doping without co-substitution, this work isolates the role of ionic size and charge effects on the $CuFe_2O_4$ lattice.

Pb-containing ferrites have been widely investigated in several magnetic oxide families, including Pb-doped spinel ferrites such as $Co_{1-x}Pb_xFe_2O_4$, garnet systems [(Pb, Th)-substituted YIG], orthoferrites (Pb-substituted $BiFeO_3$), and hexaferrites ($PbFe_{12}O_{19}$). In these studies, Pb^{2+} incorporation has been mainly associated with modifications in grain growth, electrical conductivity, magneto-optical response, or hard-magnetic anisotropy. However, these systems differ fundamentally from $CuFe_2O_4$ in terms of crystal symmetry, cation distribution, and the presence of strong Jahn–Teller distortion associated with Cu^{2+} ions. Consequently, the structural and magnetic effects induced by Pb^{2+} substitution in those ferrite families cannot be directly extended to Cu-based spinel ferrites. To the best of our knowledge, this work represents the first systematic investigation of Pb^{2+} substitution in $CuFe_2O_4$ spinel ferrite over a wide compositional range. Unlike previously reported Pb-doped $CoFe_2O_4$ or $NiFe_2O_4$ systems, Pb incorporation in $CuFe_2O_4$ leads to a distinctive tetragonal-to-pseudo-cubic structural transition driven by the suppression of Jahn–Teller distortion, accompanied by a pronounced morphology evolution and magnetic softening. To further clarify this novelty, we have added a comparative table summarizing key structural and magnetic parameters of representative Pb-containing ferrites and Pb-doped spinel systems reported in the literature and contrasted them with the present $Cu_{1-x}Pb_xFe_2O_4$ results. This comparison clearly highlights that the Pb-induced lattice relaxation, symmetry enhancement, and magnetic behavior observed here are unique to the $CuFe_2O_4$ host lattice and have not been previously reported. In this work, lead (Pb) substitution in copper spinel ferrite was carried out. The reasons for selecting this element are as follows:

- No reports have investigated the incorporation of lead in spinel ferrites, and to the best of our knowledge.
- Due to the large ionic radius of Pb (r_A = 1.19 Å) compared with that of Cu (r_A = 0.73 Å) and Fe (r_A = 0.645 Å), the synthesis of this compound is difficult and often accompanied by impurity formation—a topic that has been rarely explored.
- It can be expected that Pb in ferrite may exhibit multiferroic behavior, which could enhance the dielectric properties and increase polarization. Ferroelectric properties arise from the displacement of electrons in a solid under an external electric field. In this case, when an electric field is applied to the material, the positive Pb ions and negative oxide ions (O_2^-) are simultaneously displaced within the crystal lattice. This electron displacement leads to a change in the material's electrical behavior Based on the successful synthesis of Pb-substituted spinel ferrite samples, the samples exhibited the formation of a tetragonal structure.

2. Experimental procedures and details

2.1. Materials and synthesis

High-purity $Cu(NO_3)_2{\cdot}3H_2O$, $Pb(NO_3)_2$, and $Fe(NO_3)_3{\cdot}9H_2O$ (Merck, ≥99.9%) were used as precursors. $Cu_{1-x}Pb_xFe_2O_4$ (x = 0.0–0.30) nanoparticles were synthesized using the citrate–nitrate method. Initially, Stoichiometric proportions were mixed in deionized water with citric acid as a chelating agent. Upon heating at 80 °C under continuous stirring, a viscous gel formed. During the process, the pH of the solution was adjusted to ~7 using ammonia, allowing it to further transform into a gel. The obtained gel was then dried in an oven at 200 °C for 12 h. Finally, the dried samples were calcined in a furnace at 900 °C for 4 h to ensure phase purity.

2.2. Characterization techniques

X-ray diffraction (XRD) was performed using Cu-Kα radiation (λ = 1.5406 Å), 2θ = 20°–80°, step size 0.02°. FTIR spectroscopy was measured using a Bruker Alpha II FTIR spectrometer using KBr pellets, range 400–4000 cm^{-1}. The hysteresis loop of the samples was measured using a VSM-7300 vibrating sample magnetometer (Meghnatis Daghigh Kavir Co., Kashan, Iran) under a maximum applied magnetic field of 15 kOe at room temperature (RT).

3. Results and Discussion

3.1. XRD Structural Analysis

The X-ray diffraction (XRD) results of the $Cu_{1-x}Pb_xFe_2O_4$ (x = 0.0, 0.02, 0.04, 0.06, 0.08, 0.10, 0.15, 0.20, 0.25, and 0.30) nanoparticles are shown in Figure 1. Structural analysis confirmed that the undoped $CuFe_2O_4$ (x = 0.0) exhibited a tetragonal spinel structure belonging to the $I4_1/amd$ space group, in agreement with the standard reference pattern (ICDD No. 00-034-0425) [21]. The diffraction lines indexed to the (112), (103), (211), (202), (321), (224), and (400) planes are characteristic of the tetragonal symmetry. A gradual shift of these peaks toward lower diffraction angles is observed upon Pb^{2+} substitution, implying lattice expansion caused by the larger ionic radius of Pb^{2+} (CN6 =1.19 Å) compared with those of Cu^{2+} (CN6 =0.73 Å) and Fe^{3+} (CN6 =0.645 Å) [22-23].

As the Pb content increases beyond x = 0.15, a progressive merging of diffraction peaks becomes evident, indicating that the lattice undergoes a transition from the tetragonal phase to a pseudo-cubic configuration. This evolution reflects structural rearrangements in cation positions between tetrahedral (A) and octahedral (B) sites, along with relaxation of the Jahn–Teller distortion. The gradual change in the Bragg reflections suggests a continuous increase in structural symmetry as the Pb^{2+} concentration rises [24].

No secondary phases are observed up to x = 0.20, confirming that Pb^{2+} ions are effectively incorporated into the spinel lattice at moderate doping levels. However, for higher substitutions ($x \geq 0.25$), the emergence of weak peaks near $2\theta \approx 33°$ and 36° corresponds to traces of $PbFe_{12}O_{19}$ (JCPDS No. 84-0757), indicating that excessive Pb causes partial decomposition of the spinel structure. The formation of this phase can be attributed to the lattice strain and charge imbalance introduced by the oversaturation of Pb ions. This behavior is further explained by the large ionic radius of Pb^{2+} compared to Fe^{3+}, which induces significant lattice strain at higher concentrations. Additionally, the charge imbalance introduced by Pb^{2+} substitution destabilizes the spinel framework when the substitution level exceeds x = 0.20, promoting partial decomposition and segregation of a Pb-rich hexaferrite phase. These effects collectively identify x = 0.25 as a critical composition, beyond which the spinel structure can no longer accommodate Pb ions without structural relaxation via secondary phase formation.

The calculated lattice parameters (a and c) listed in Table 1 show a steady increase with Pb content, evidencing unit-cell expansion as Pb^{2+} enters the crystal lattice. During the gradual transformation from the tetragonal ($a = b < c$) to the cubic ($a = b = c$) symmetry, the c-axis parameter decreases while the a-axis expands, leading to a reduced c/a ratio that signifies the diminishing Jahn–Teller effect [25]. This structural adjustment affects the Fe–O and Cu–O bond geometry, which consequently modify the magnetic and optical properties of the Pb-doped ferrites.

Pb^{2+} ions are likely to occupy octahedral (B) sites, where they disrupt the Cu^{2+}/Fe^{3+} arrangement and promote cation redistribution between A and B positions. The incorporation of these larger cations generates local lattice strain and suppresses anisotropic distortion, thereby stabilizing a more symmetric spinel framework at higher doping levels. The altered Fe^{3+}–O^{2-}–Fe^{3+} superexchange pathways and varying bond lengths are expected to soften the magnetic behavior and influence the dielectric response of the $Cu_{1-x}Pb_xFe_2O_4$ nanostructures [25].

The monotonic increase in lattice constant is attributed to the replacement of smaller Cu^{2+} (0.73 Å) by larger Pb^{2+} (1.29 Å) ions at octahedral sites, causing expansion of the crystal lattice. The reduction in crystallite size suggests that Pb acts as a growth inhibitor, introducing local strain and defect concentration, thereby lowering grain coalescence during calcination. The observed trend agrees with Vegard's law for $x \leq 0.2$, confirming successful substitution.

In our previous investigations, we consistently demonstrated that cation substitution at the A and B sites induces a tetragonal-to-cubic structural transition, accompanied by clear changes in lattice parameters, magnetic ordering, and saturation magnetization. For example:

- In Zn/Cr co-substituted $CuFe_2O_4$ spinels, we showed that substitution-induced cation redistribution suppresses Jahn–Teller distortion, driving a structural modification and enhancing ferrimagnetism [3].
- A direct correlation between structural phase transition and magnetic behavior was established in Co^{2+}/Gd^{3+} co-substituted copper ferrites, where the evolution from tetragonal to cubic symmetry was linked to the redistribution of cations between tetrahedral and octahedral sites [25].
- Similar structure–property correlations were reported in Ni–Cu–Zn spinel ferrites, confirming that compositional tuning modifies cation occupancy and magnetic interactions in spinel lattices [21].
- Our recent studies on Zn/Fe, Zn/Co, and Ni/La co-substituted $CuFe_2O_4$ ferrites further demonstrated that changes in lattice symmetry, unit-cell volume, and magnetic parameters originate from systematic cation substitution and redistribution effects, even in the absence of Mössbauer analysis [6,8,12].

Based on these consistent findings across multiple substitution systems, the structural changes and phase transition discussed in the present manuscript are interpreted within a well-established framework, rather than as isolated observations. To address the reviewer's concern, we have revised the manuscript to (i) strengthen the discussion by explicitly citing these prior studies, and (ii) adopt a more cautious wording where appropriate, clearly stating that the proposed cation redistribution model is inferred from structural trends and magnetic behavior.

The average crystallite size (D) and lattice microstrain (ε) were determined using the Williamson–Hall (W–H) method, which separates the effects of size and strain broadening in XRD peak profiles [26].

The corrected full width at half maximum (FWHM) of diffraction peaks (β) is related to D and ε through the following equation [27]:

$$\beta\cos\theta = \frac{k\lambda}{D} + 4\varepsilon\sin\theta \quad (1)$$

where β is the instrumentally corrected FWHM in radians, λ is the X-ray wavelength (1.5406 Å for Cu-Kα radiation), k is the shape factor (typically 0.94), D is the average crystallite size, ε is the lattice microstrain, and θ is the Bragg diffraction angle. By plotting $\beta\cos\theta$ versus $4\sin\theta$, a linear relationship is obtained in which the slope gives the microstrain (ε) and the intercept yields $k\lambda/D$. The main diffraction peaks, such as (112), (103), (211), (321), and (224), were employed for the W–H analysis to obtain accurate estimates of D and ε. The strain-induced broadening of diffraction peaks, quantified using the Williamson–Hall method, show a proportional rise with Pb content for x up to 0.2, supporting increased lattice distortion.

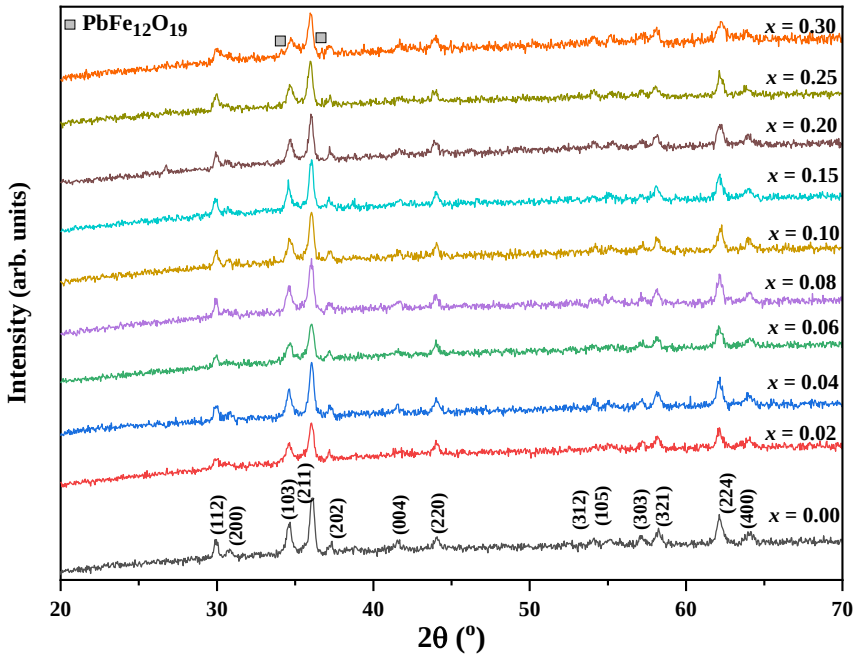

Fig. 1. XRD pattern of $Cu_{1-x}Pb_xFe_2O_4$ ferrites.

Table 1. Crystallographic parameters of $Cu_{1-x}Pb_xFe_2O_4$ nanoparticles.

Samples	Lattice parameters			*c/a*	*V*	ρ_{XRD}	*D*	*ε*
	a (Å)	*a** (Å)	*c* (Å)		(Å^3)	(g/cm^3)	(nm)	(10^{-3})
x = 0.00	5.797	8.198	8.646	1.492	290.50	5.48	25	1.2
x = 0.02	5.803	8.207	8.637	1.488	291.00	5.55	22	1.5
x = 0.04	5.810	8.217	8.626	1.485	291.47	5.65	22	1.9
x = 0.06	5.818	8.228	8.617	1.480	292.00	5.70	20	2.2
x = 0.08	5.825	8.238	8.608	1.477	292.50	5.76	18	2.5
x = 0.10	5.834	8.250	8.600	1.473	293.00	5.81	15	3.0
x = 0.15	5.855	8.280	8.578	1.464	294.00	5.89	12	4.5
x = 0.20	5.876	8.310	8.552	1.455	295.10	5.97	11	3.5
x = 0.25	5.890	8.330	8.482	1.440	294.20	5.97	13	2.5
x = 0.30	5.904	8.349	8.465	1.433	294.80	6.07	14	3.0

3.2. Morphology

Panel A in Figure 2 presents the FESEM images of the $Cu_{1-x}Pb_xFe_2O_4$ samples with different Pb substitution levels: (a) *x* = 0.00, (b) *x* = 0.10, (c) *x* = 0.20, and (d) *x* = 0.30, all recorded at a scale bar of 2 μm. Additional high-magnification images are shown for the *x* = 0.20 sample at a scale bar of 200 nm (Fig. 2e) and for the *x* = 0.30 sample at 500 nm (Fig. 2f). Panel (B) displays the elemental mapping images of the *x* = 0.30 sample, confirming the presence and uniform spatial distribution of Fe, Cu, O, and Pb elements. The pristine $CuFe_2O_4$ sample (*x* = 0.00) exhibits a morphology composed of stacked nanosheet-like structures, which aggregate into irregularly shaped and highly agglomerated microparticles. This morphology is commonly observed in copper ferrites and is attributed to anisotropic crystal growth and strong magnetic dipole–dipole interactions between particles during synthesis. With the introduction of Pb^{2+} ions at a substitution level of *x* = 0.10, a noticeable morphological transformation occurs. The initially irregular aggregates begin to evolve into more defined microparticles with truncated square-pyramid geometries. This change can be attributed to the partial replacement of Cu^{2+} ions (ionic radius ≈ 0.73 Å) by larger Pb^{2+} ions (ionic radius ≈ 1.19 Å), which induces lattice distortion, modifies surface energy, and alters the relative growth rates of different crystallographic planes [23].

At a higher substitution level (*x* = 0.20), the morphology becomes more uniform, with most particles adopting well-defined truncated square-pyramid shapes. This suggests that Pb substitution increasingly stabilizes specific crystal facets, promoting more controlled and directional crystal growth. The suppression of random agglomeration at this stage indicates an improvement in nucleation–growth balance and a reduction in surface defects. For the highest Pb content (*x* = 0.30), the microparticles predominantly consist of square–pyramidal units that are preferentially attached through their basal faces, leading to the formation of well-defined octahedral-like assemblies. This hierarchical self-assembly behavior can be explained by enhanced facet–facet interactions and minimized total surface energy in the presence of Pb-induced lattice strain and modified bonding characteristics at the particle interfaces. Overall, the progressive substitution of Pb^{2+} ions for Cu^{2+} ions plays a crucial role in tuning the morphology of $Cu_{1-x}Pb_xFe_2O_4$ ferrites, driving a systematic

transition from irregular nanosheet-based aggregates to ordered polyhedral microstructures. Such morphological evolution is expected to significantly influence the functional properties of the material, particularly surface reactivity, ion diffusion pathways, and electrochemical performance. Furthermore, the elemental mapping results (Panel B in Fig. 2) clearly demonstrate the homogeneous distribution of Fe, Cu, O, and Pb throughout the x = 0.30 sample, indicating successful incorporation of Pb into the ferrite lattice without detectable phase segregation or elemental clustering. This uniform elemental distribution further supports the structural integrity and compositional stability of the synthesized Pb-substituted copper ferrites.

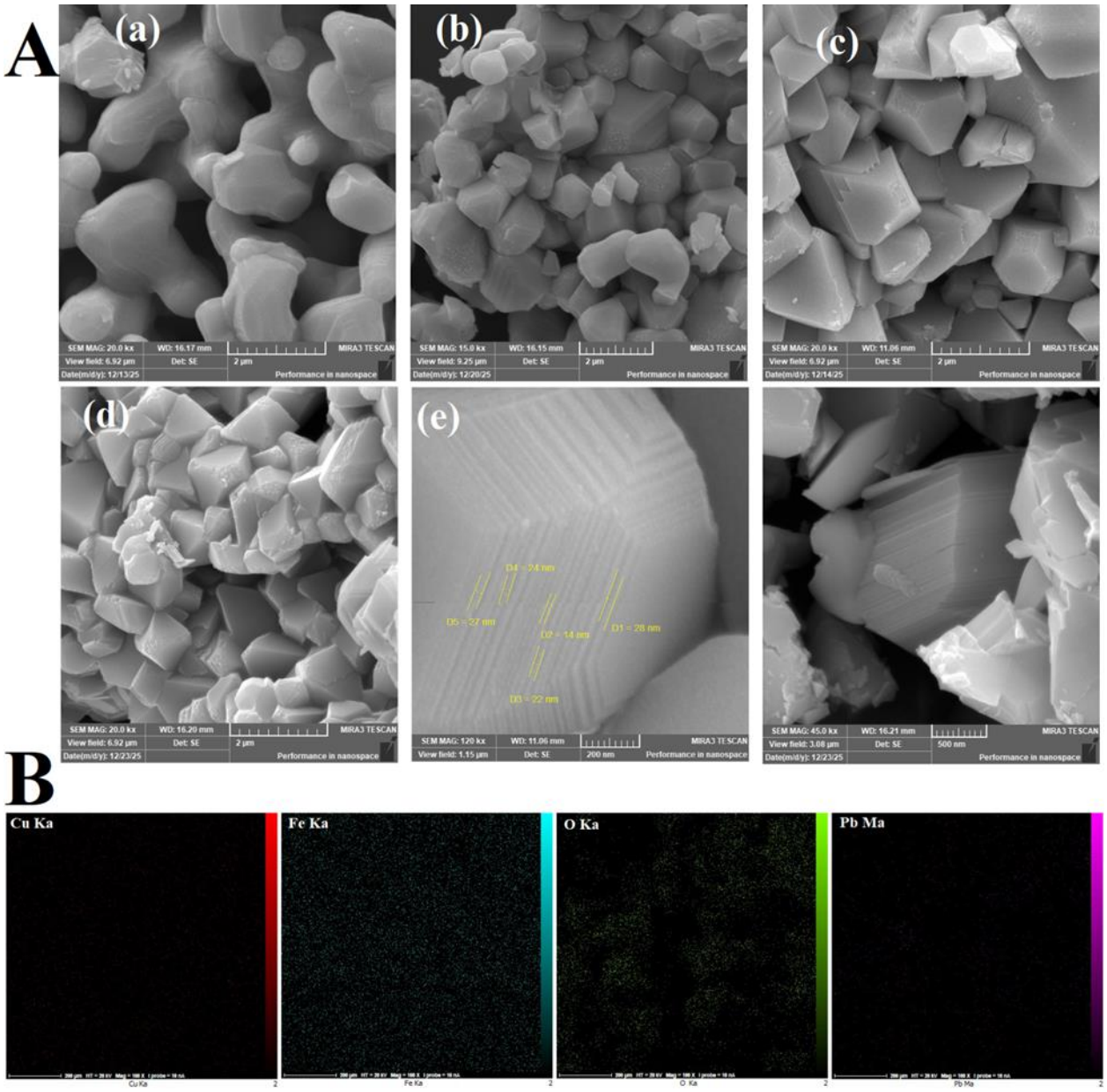

Fig. 2. Panel (A) shows FESEM images of the $Cu_{1-x}Pb_xFe_2O_4$ samples: (a) x = 0.00, (b) x = 0.10, (c) x = 0.20, and (d) x = 0.30, all recorded at a scale bar of 2 µm. FESEM images of (e) x = 0.20 sample at a higher magnification with a scale bar of 200 nm, and (f) for x = 0.30 sample at a scale bar of 500 nm. Panel (B) displays the elemental mapping images of the x = 0.30 sample, confirming the presence and homogeneous distribution of Fe, Cu, O, and Pb elements.

3.3. FTIR Analysis

FTIR spectra of $Cu_{1-x}Pb_xFe_2O_4$ samples are shown in Figure 3. They display two prominent absorption bands: $\nu_A \approx 602$ cm^{-1}, corresponding to Fe–O stretching vibrations in tetrahedral sites, and $\nu_B \approx 442$ cm^{-1}, associated with Fe–O (and Cu–O) stretching in octahedral sites. A consistent shift of both ν_A and ν_B toward lower frequencies indicates lengthening of the M–O bond due to lattice expansion from Pb incorporation [27-28]. Furthermore, band broadening and intensity reduction at higher Pb levels reveal increased structural disorder. The preservation of both bands confirms that the fundamental spinel framework remains intact up to x = 0.3.

The infrared absorption bands of spinel ferrites arise from the stretching vibrations of metal–oxygen bonds at the tetrahedral (A) and octahedral (B) sites. The vibrational frequency (ν) of these modes can be approximately expressed as:

$$\nu \propto \sqrt{\frac{k}{\mu}} \quad (2)$$

where k is the force constant of the M–O bond and μ is the reduced mass of the vibrating system. Therefore, a decrease in wavenumber may result from either an increase in μ (due to the substitution of a heavier cation) or a decrease in k (due to bond weakening), or a combination of both effects. In the present system, when Pb^{2+} ions are substituted for Cu^{2+} in $Cu_{1-x}Pb_xFe_2O_4$, both the tetrahedral and octahedral absorption bands in the FTIR spectra shift toward lower wavenumbers by approximately 10 cm^{-1}. The nearly equal shift of both bands suggests that Pb substitution affects the bonding environment of both A and B sites similarly. This observation indicates that Pb^{2+} ions are likely distributed over both tetrahedral and octahedral sites, rather than being confined to only one type of site. Considering the significantly larger ionic radius of Pb^{2+} compared to Cu^{2+}, the incorporation of Pb^{2+} may introduce lattice distortion and elongate the metal–oxygen bonds, thereby reducing the bond force constant k throughout the lattice. Furthermore, partial redistribution of Fe^{3+} ions between the A and B sites (a change in the inversion parameter) may also occur to maintain charge balance and structural stability, further influencing both vibrational modes. A simple estimation based on the change in reduced mass (μ) shows that a complete replacement of Cu^{2+} by Pb^{2+} would theoretically cause a much larger frequency shift than the observed 10 cm^{-1}. Hence, the experimental shift can be explained by a partial substitution of Pb^{2+} at both sites-approximately 20% occupation of the specific site could produce such a moderate shift if mass effects dominate. This supports a mixed cation distribution model for Pb^{2+} ions in $Cu_{1-x}Pb_xFe_2O_4$. In summary, the comparable downward shift of both tetrahedral and octahedral vibrational bands in the FTIR spectra indicates that Pb^{2+} ions are partially distributed over both cationic sublattices, resulting in a simultaneous increase in reduced mass and decrease in bond force constant, leading to the observed red shift of about 10 cm^{-1}.

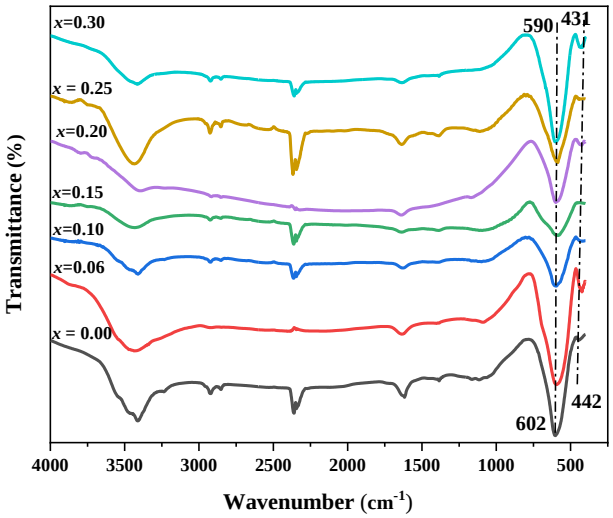

Fig. 3 FTIR spectra of $Cu_{1-x}Pb_xFe_2O_4$ ferrites.

3.4. Magnetic Properties

Fig. 4 shows the hysteresis loops of $Cu_{1-x}Pb_xFe_2O_4$ samples recorded at room temperature. The magnetic hysteresis loops display soft-ferromagnetic behavior with narrow loops and low coercivity. The quantitative parameters are summarized in Table 2. The saturation magnetization (M_s) values were derived using the law of approach to saturation (LAS) as shown in Figure 5. In high magnetic fields, the experimental data were fitted using the empirical relation [27,29]:

$$M(H) = M_s\,[1 - (b/H^2) - (c/H^3)] \quad (3)$$

where *M(H)* represents the magnetization at field *H*, and *b* and *c* are constants proportional to K_1^2 and K_1^3, respectively (K_1 is the first-order magnetocrystalline anisotropy constant). The magnetic parameters obtained from LAS fitting are summarized in Table 2. In the case of a cubic crystal structure, the H_a is directly proportional to the first-order magnetocrystalline anisotropy constant K_1, which is determined by the coefficient b as follows [25]:

$$K_1 = \frac{105}{8} b M_s^2 \quad (4)$$

From Table 2, the K_1 values increase with the Pb^{2+} co-substitution. Higher values of K_1 indicate that the desired material has magnetic moments that strongly depend on a specific direction.

A gradual incorporation of Pb^{2+} ions in place of Cu^{2+} results in a noticeable increase in M_s up to $x = 0.25$, followed by a slight decline at higher Pb contents. This magnetic behavior reflects a progressive modification of the cation distribution within the spinel lattice. According to the Néel two-sublattice model, the net magnetization (M) of ferrites is expressed as [30-31]:

$$M = M_B - M_A \quad (5)$$

where M_A and M_B correspond to the magnetic moments of cations at the tetrahedral (A) and octahedral (B) sites, respectively. The antiparallel alignment of spins between these sublattices gives rise to the observed ferrimagnetic behavior.

In pure $CuFe_2O_4$, Fe^{3+} ions (5.9 μ_B) occupy both A and B sites, while Cu^{2+} ions (1.9 μ_B) primarily reside at octahedral sites [32-34]. Pb^{2+} ions, being diamagnetic (0 μ_B) with an ionic radius significantly larger than Cu^{2+}, primarily influence the magnetic properties indirectly through structural distortion and cation rearrangement rather than through direct magnetic contributions. The substitution of diamagnetic Pb^{2+} ions for Cu^{2+} modifies this distribution and the local superexchange interactions. As Pb^{2+} enters the B-sublattice, its larger ionic radius weakens Fe^{3+}–O^{2-}–Fe^{3+} and Fe^{3+}–O^{2-}–Cu^{2+} exchange pathways, reducing magnetocrystalline anisotropy and facilitating easier domain wall motion [35-36]. This leads to a marked reduction in coercivity (H_c) while maintaining moderate M_s values for compositions up to $x = 0.25$.

At low Pb substitution levels, the small fraction of Pb^{2+} ions entering the B-sites can induce partial redistribution of Fe^{3+} ions toward the tetrahedral sublattice. This redistribution enhances Fe^{3+}(B)–O^{2-}–Fe^{3+}(A) superexchange coupling, strengthening $M_B - M_A$ and thus increasing the net M_s [37-38]. However, beyond $x \approx 0.25$, excessive Pb incorporation introduces lattice strain and possible $PbFe_{12}O_{19}$ secondary phase formation, which disrupts long-range magnetic ordering. $PbFe_{12}O_{19}$ dilutes

the ferrimagnetic matrix, leading to decreased M_s and H_c values at higher substitution levels.

The observed softening of magnetic hysteresis with Pb content corresponds to a decrease in magnetocrystalline anisotropy and a relaxation of Jahn–Teller distortion associated with Cu^{2+}. The substitution of non-Jahn–Teller Pb^{2+} stabilizes a more symmetric (quasi-cubic) spinel lattice, favoring domain wall mobility and lowering coercivity. The combined effects of non-magnetic Pb^{2+} substitution, weakened Fe^{3+}–O^{2-}–Fe^{3+} exchange, and lattice relaxation collectively promote a soft magnetic character in Pb-doped $CuFe_2O_4$ ferrites.

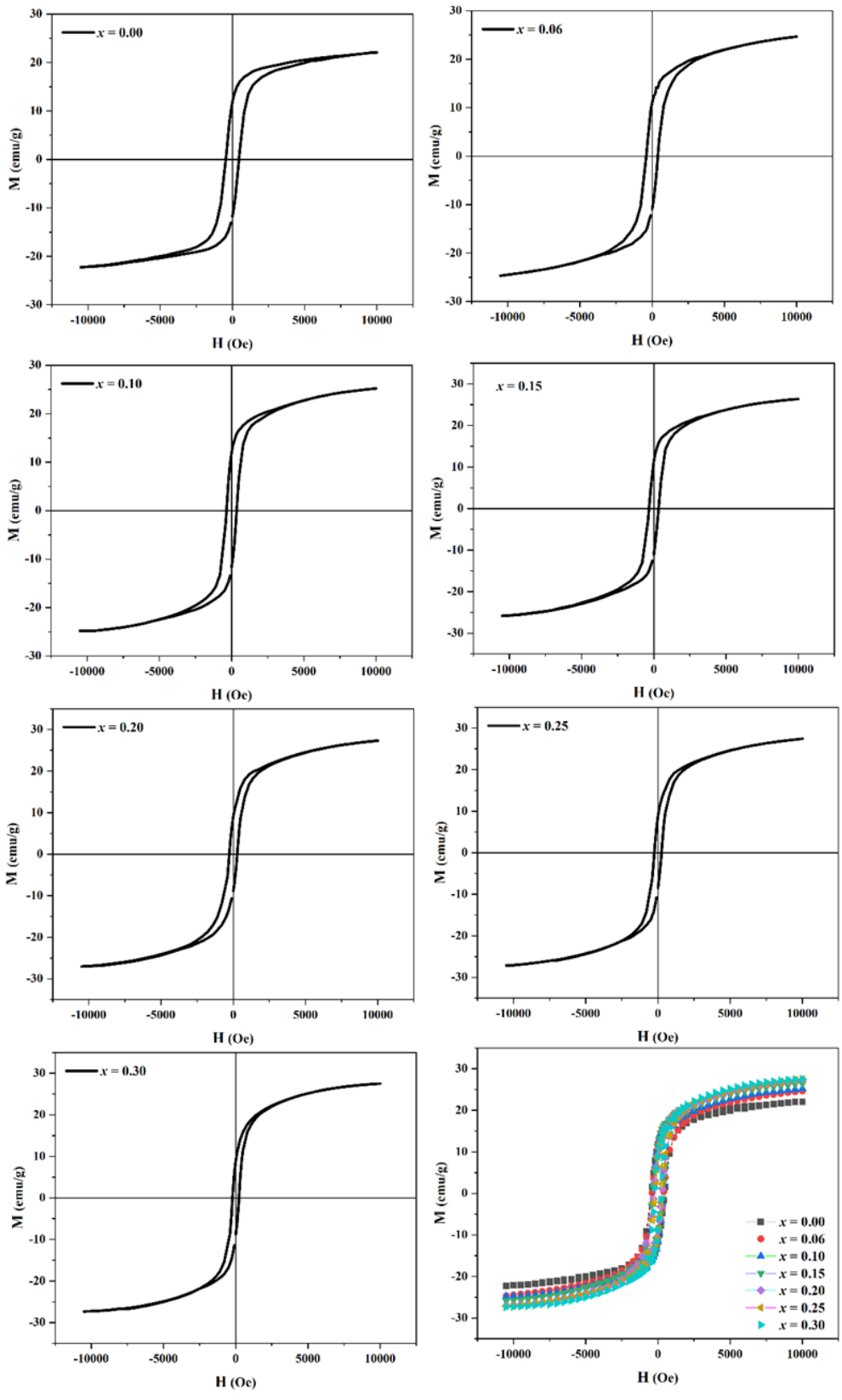

Fig. 4. Hysteresis loops of the $Cu_{1-x}Pb_xFe_2O_4$ ferrites.

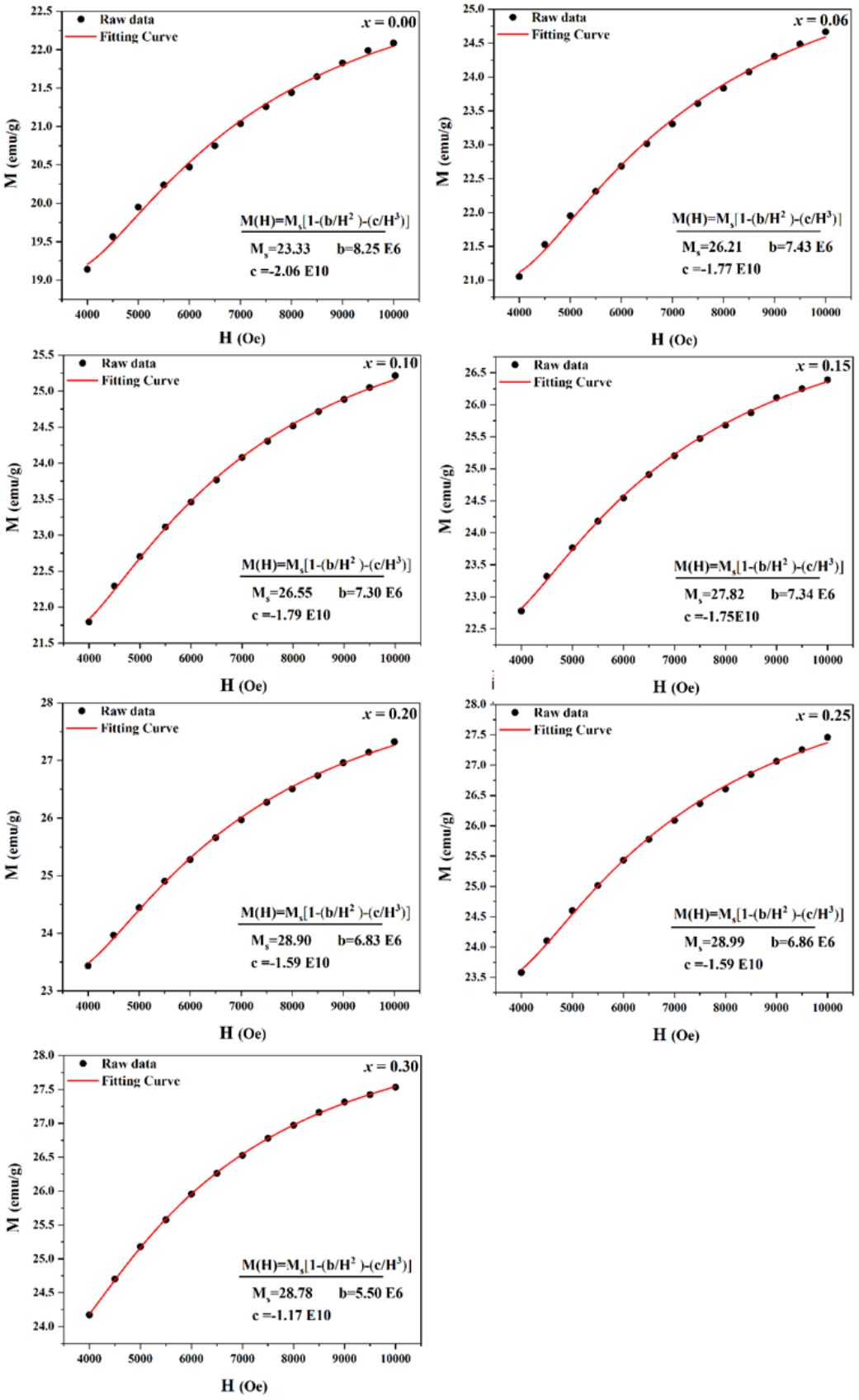

Fig. 5. LAS curves of $Cu_{1-x}Pb_xFe_2O_4$ ferrites.

Table 2. Magnetic parameters of $Cu_{1-x}Pb_xFe_2O_4$.

Sample	M_s(emu/g)	M_r(emu/g)	H_c(Oe)	M_r/M_s	$b*10^{-6}$	$-c*10^{-10}$	K_1*10^{-6}(emu/cm^3)
x = 0.00	23.33	11.98	448	0.513	8.25	2.06	1.33
x = 0.06	26.21	11.05	380	0.422	7.43	1.77	1.47
x = 0.10	26.55	11.15	350	0.420	7.30	1.79	1.51
x = 0.15	27.82	11.10	330	0.399	7.34	1.75	1.61
x = 0.20	28.90	8.95	278	0.310	6.83	1.59	1.63
x = 0.25	28.99	8.90	260	0.307	6.86	1.59	1.64
x = 0.30	28.78	8.90	245	0.309	5.50	1.17	1.48

4. Conclusions

XRD analysis confirmed successful Pb incorporation into the $CuFe_2O_4$ spinel lattice up to x = 0.20 without secondary phase formation. The diffraction peaks shifted toward lower 2θ values with increasing Pb content, indicating lattice expansion due to the larger ionic radius of Pb^{2+}. Beyond $x \geq 0.25$, minor peaks of $PbFe_{12}O_{19}$ appeared, evidencing partial phase decomposition. The c/a ratio decreased steadily with Pb doping, signifying suppression of Jahn–Teller distortion and a progressive transformation from tetragonal to quasi-cubic symmetry. FTIR spectra displayed two characteristic absorption bands near 602 and 442 cm^{-1}, corresponding to metal–oxygen stretching vibrations at tetrahedral (A) and octahedral (B) sites, respectively. Both bands shifted to lower frequencies with Pb incorporation, confirming lattice expansion and altered cation distribution. Magnetic hysteresis loops revealed soft ferromagnetic behavior across all compositions. The saturation magnetization increased with Pb substitution up to x = 0.25, attributed to enhanced Fe^{3+}(B)–O^{2-}–Fe^{3+}(A) superexchange interactions due to cation redistribution. A further increase in Pb concentration reduced M_s and Hc, correlating with lattice strain and impurity phase formation. The overall magnetic softening with Pb content reflects decreased anisotropy and relaxation of Jahn–Teller effects. These findings demonstrate that Pb^{2+} substitution in $CuFe_2O_4$ effectively tailors the structural symmetry, cation distribution, and magnetic response, opening prospects for multifunctional ferrites with tunable magnetostructural characteristics.

Funding Statement

This research received no specific grant from any funding agency.

Conflicts of interest

The authors declare that they have no known competing financial interests or personal relationships that could have appeared to influence the work reported in this paper.

Authors contribution statement

Sanaz Rezaei: Formal Analysis, Resources, Methodology, Data Curation.

Ahmad Gholizadeh: Resources, Methodology, Data Curation, Writing - Original Draft, Writing - Review & Editing, Supervision.

Muhammad Atif: Writing - Review & Editing, Supervision.

References

[1] Salih, S.J. and Mahmood, W.M., 2023. Review on magnetic spinel ferrite (MFe_2O_4) nanoparticles: From synthesis to application. *Heliyon*, *9*(6).

[2] Dippong, T., Levei, E.A. and Cadar, O., 2022. Investigation of structural, morphological and magnetic properties of MFe_2O_4 (M= Co, Ni, Zn, Cu, Mn) obtained by thermal decomposition. *International Journal of Molecular Sciences*, *23*(15), p.8483.

[3] Gholizadeh, A. and Hosseini, S., 2025. Structural Modification and Enhanced Ferrimagnetism of Zn/Cr Co-Substituted $CuFe_2O_4$ Spinels through Sol–Gel Synthesis. *physica status solidi (a)*, p.2400901.

[4] Tarantino, S.C., Giannini, M., Carpenter, M.A. and Zema, M., 2016. Cooperative Jahn–Teller effect and the role of strain in the tetragonal-to-cubic phase transition in $MgxCu_{1-x}Cr_2O_4$. *IUCrJ*, *3*(5), pp.354-366.

[5] Kyono, A., Gramsch, S.A., Nakamoto, Y., Sakata, M., Kato, M., Tamura, T. and Yamanaka, T., 2015. High-pressure behavior of cuprospinel $CuFe_2O_4$: Influence of the Jahn-Teller effect on the spinel structure. *American Mineralogist*, *100*(8-9), pp.1752-1761.

[6] Gholizadeh, A. and Hamrah, H., 2025. $Cu_{1-x}Ni_xFe_{2-x}La_xO_4$ ferrites: a synergetic impact of Ni/La co-substitution on enhancement of magnetic properties. *Journal of Sol-Gel Science and Technology*, 116(1), pp.520–534.

[7] Caddeo, F., Loche, D., Casula, M.F. and Corrias, A., 2018. Evidence of a cubic iron sub-lattice in t-$CuFe_2O_4$ demonstrated by X-ray Absorption Fine Structure. *Scientific Reports*, *8*(1), p.797.

[8] Gholizadeh, A. and Hosseini, 2025. S. Zn/Co co-substitution: Tuning the physical properties of $CuFe_2O_4$ nanoparticles. *Journal of Sol-Gel Science and Technology,* 116(1), pp.508–519.

[9] Xian, G., Kong, S., Li, Q., Zhang, G., Zhou, N., Du, H. and Niu, L., 2020. Synthesis of spinel ferrite MFe_2O_4 (M= Co, Cu, Mn, and

Zn) for persulfate activation to remove aqueous organics: effects of M-site metal and synthetic method. *Frontiers in chemistry*, *8*, p.177.

[10] Zohrabi, Y., 2024. Synthesis and application of magnetic ferrites (MFe_2O_4) in the removal of heavy metals from aqueous solutions: an updated review. *Materials Science and Engineering: B*, *299*, p.117024.

[11] Hua, J., Cheng, Z., Chen, Z., Dong, H., Li, P. and Wang, J., 2021. Tuning the microstructural and magnetic properties of $CoFe_2O_4/SiO_2$ nanocomposites by Cu^{2+} doping. *RSC advances*, *11*(42), pp.26336-26343.

[12] Gholizadeh, A. and Hosseini, S., 2025. A synergetic impact of Zn/Fe co-substitution on enhancement physical properties of copper spinel ferrite. *Journal of Sol-Gel Science and Technology* 116(1), pp.154–165.

[13] Gabal, M.A., Katowah, D.F., Hussein, M.A., Al-Juaid, A.A., Awad, A., Abdel-Daiem, A.M., Saeed, A., Hessien, M.M. and Asiri, A.M., 2021. Structural and magnetoelectrical properties of MFe_2O_4 (M= Co, Ni, Cu, Mg, and Zn) ferrospinels synthesized via an egg-white biotemplate. *ACS omega*, *6*(34), pp.22180-22187.

[14] Zhang, R., Qin, C., Bala, H., Wang, Y. and Cao, J., 2023. Recent progress in spinel ferrite (MFe_2O_4) chemiresistive based gas sensors. *Nanomaterials*, *13*(15), p.2188.

[15] Humbe, A.V., Kounsalye, J.S., Somvanshi, S.B., Kumar, A. and Jadhav, K.M., 2020. Cation distribution, magnetic and hyperfine interaction studies of Ni–Zn spinel ferrites: role of Jahn Teller ion (Cu^{2+}) substitution. *Materials Advances*, *1*(4), pp.880-890.

[16] Ansari, S.M., Ghosh, K.C., Devan, R.S., Sen, D., Sastry, P.U., Kolekar, Y.D. and Ramana, C.V., 2020. Eco-friendly synthesis, crystal chemistry, and magnetic properties of manganese-substituted $CoFe_2O_4$ nanoparticles. *ACS omega*, *5*(31), pp.19315-19330.

[17] Rajenimbalkar, R.S., Deshmukh, V.J., Patankar, K.K. and Somvanshi, S.B., 2024. Effect of multivalent ion doping on magnetic, electrical, and dielectric properties of nickel ferrite nanoparticles. *Scientific Reports*, *14*(1), p.29547.

[18] Dippong, T., Deac, I.G., Cadar, O., Levei, E.A. and Petean, I., 2020. Impact of Cu^{2+} substitution by Co^{2+} on the structural and magnetic properties of $CuFe_2O_4$ synthesized by sol-gel route. *Materials Characterization*, *163*, p.110248.

[19] Pawar, D.B., Khirade, P.P., Vinayak, V., Ravangave, L.S. and Rathod, S.M., 2020. Sol–gel auto-ignition fabrication of Gd3+ incorporated $Ni_{0.5}Co_{0.5}Fe_2O_4$ multifunctional spinel ferrite nanocrystals and its impact on structural, optical and magnetic properties. *SN applied sciences*, *2*(10), p.1713.

[20] Sefatgol, R., Gholizadeh, A. and Hatefi, H., 2025. Enhancement of magnetic properties of bismuth-substituted Mn-Mg-Cu-Zn ferrite prepared by sol-gel route. *Journal of Sol-Gel Science and Technology*, *116*(1), pp.90-103.

[21] Takalloo, F., Gholizadeh, A. and Ardyanian, M., 2024. Crystal structure-physical properties correlation in Ni–Cu–Zn spinel ferrite. *Journal of Materials Science: Materials in Electronics*, *35*(27), p.1792.

[22] Benali, A., Saher, L., Bejar, M., Dhahri, E., Graca, M.F.P., Valente, M.A., Sanguino, P., Helguero, L.A., Bachari, K., Silva, A.M. and Costa, B.F.O., 2023. $CoFe_2O_4$ spinel ferrite studies on permanent magnet application and cytotoxic effects on breast and prostate cancer cell lines. *Journal of Materials Science: Materials in Electronics*, *34*(1), p.53.

[23] Shannon, R.T. and Prewitt, C.T., 1969. Effective ionic radii in oxides and fluorides. *Structural Science*, *25*(5), pp.925-946.

[24] Marinca, T.F., Chicinaş, I. and Isnard, O., 2013. Structural and magnetic properties of the copper ferrite obtained by reactive milling and heat treatment. *Ceramics International*, *39*(4), pp.4179-4186.

[25] Choupani, M. and Gholizadeh, A., 2024. Correlation between structural phase transition and physical properties of Co^{2+}/Gd^{3+} co-substituted copper ferrite. *Journal of Rare Earths*, *42*(7), pp.1344-1353.

[26] Pan, L. and Xu, B., 2013. Synthesis of spinel-structure $CuFe_2O_4$ nanoparticles and their effective electrocatalysis properties. *JOM*, *65*(6), pp.695-701.

[27] Gholizadeh, A., 2017. A comparative study of physical properties in Fe_3O_4 nanoparticles prepared by coprecipitation and citrate methods. *Journal of the american ceramic society*, *100*(8), pp.3577-3588.

[28] Satheeshkumar, M.K., Kumar, E.R., Srinivas, C., Prasad, G., Meena, S.S., Pradeep, I., Suriyanarayanan, N. and Sastry, D.L., 2019. Structural and magnetic properties of $CuFe_2O_4$ ferrite nanoparticles synthesized by cow urine assisted combustion method. *Journal of Magnetism and Magnetic Materials*, *484*, pp.120-125.

[29] Jasim, S.A., Patra, I., Opulencia, M.J.C., Hachem, K., Parra, R.M.R., Ansari, M.J., Jalil, A.T., Al-Gazally, M.E., Naderifar, M., Khatami, M. and Akhavan-Sigari, R., 2022. Green synthesis of spinel copper ferrite ($CuFe_2O_4$) nanoparticles and their toxicity. *Nanotechnology Reviews*, *11*(1), pp.2483-2492.

[30] Eghdami, F. and Gholizadeh, A., 2023. A correlation between microstructural and impedance properties of $MnFe_{2-x}Co_xO_4$ nanoparticles. *Physica B: Condensed Matter*, *650*, p.414551.

[31] Mulud, F.H., Dahham, N.A. and Waheed, I.F., 2020, November. Synthesis and characterization of copper ferrite nanoparticles. In *IOP Conference Series: Materials Science and Engineering* (Vol. 928, No. 7, p. 072125). IOP Publishing.

[32] Spaldin, N.A., 2011. *Magnetic materials: fundamentals and applications*. Cambridge university press.

[33] Hamrah, H. and Gholizadeh, A., 2025. Exploring Bismuth-Induced Structural Modifications and Magnetic Phase Transitions in $CuFe_2O_4$ Ferrite. *Progress in Physics of Applied Materials*, *5*(2), pp.107-117.

[34] Gholizadeh, A. and Hosseini, S., 2026. Structural and Magnetic Phase Transitions in $Cu_{1-3x}Zn_{2x}MnxFe_2O_4$ Ferrites. *Progress in Physics of Applied Materials*, *6*(1), pp.1-13.

[35] Gholizadeh, A. and Jafari, E., 2017. Effects of sintering atmosphere and temperature on structural and magnetic properties of Ni-Cu-Zn ferrite nano-particles: Magnetic enhancement by a reducing atmosphere. *Journal of Magnetism and Magnetic Materials*, *422*, pp.328-336.

[36] Gholizadeh, A., 2018. A comparative study of the physical properties of Cu-Zn ferrites annealed under different atmospheres and temperatures: Magnetic enhancement of $Cu_{0.5}Zn_{0.5}Fe_2O_4$ nanoparticles by a reducing atmosphere. *Journal of Magnetism and Magnetic Materials*, *452*, pp.389-397.

[37] Gholizadeh, A. and Beyranvand, M., 2020. Investigation on the structural, magnetic, dielectric and impedance analysis

of $Mg_{0.3-x}Ba_xCu_{0.2}Zn_{0.5}Fe_2O_4$ nanoparticles. *Physica B: Condensed Matter*, *584*, p.412079.

[38] Sayyar, S., Aslibeiki, B. and Asgari, A., 2022. $CoFe_2O_4$ bulk, nanoparticles and layer: A comparison of structural, magnetic, and optical properties. *Progress in Physics of Applied Materials*, *2*(2), pp.165-173.